Atmos. Chem. Phys. Discuss., 8, 18111–18153, 2008
www.atmos-chem-phys-discuss.net/8/18111/2008/

Atmospheric
Chemistry
and Physics
Discussions

Sensitivity of satellite observations for freshly produced lightning NO_x

S. Beirle[1], M. Salzmann[2], M. G. Lawrence[1], and T. Wagner[1]

[1]Max-Planck-Institut für Chemie, (Otto Hahn Institute), Mainz, Germany
[2]Princeton University, New Jersey, NJ, USA

Received: 12 August 2008 – Accepted: 28 August 2008 – Published: 15 October 2008

Correspondence to: S. Beirle (beirle@mpch-mainz.mpg.de)

Published by Copernicus Publications on behalf of the European Geosciences Union.

Abstract

In this study, we analyse the sensitivity of nadir viewing satellite observations in the visible range to freshly produced lightning NO_x, i.e. for meteorological and (photo-) chemical conditions found in and around cumulonimbus clouds. For the first time, such a study is performed accounting for photo-chemistry, dynamics, and radiative transfer in a consistent way: A one week episode in the TOGA COARE/CEPEX region (Pacific) in December 1992 is simulated with a 3-D cloud resolving chemistry model. The simulated hydrometeor mixing ratios are fed into a Monte Carlo radiative transfer model to calculate box-Air Mass Factors (box-AMFs) for NO_2. From these box-AMFs, together with model NO_x profiles, slant columns of NO_2 (S^{NO_2}), i.e. synthetic satellite measurements, are calculated and set in relation to the actual model NO_x vertical column (V^{NO_x}), yielding the "sensitivity" S^{NO_2}/V^{NO_x}.

From this study, we find a mean sensitivity of 0.46. NO_x below the cloud bottom is mostly present as NO_2, but shielded from the satellites' view, whereas NO_x at the cloud top or above is shifted to NO due to high photolysis and low temperature, and hence not detectable from space. But a significant fraction of the lightning produced NO_x in the middle part of the cloud is present as NO_2 and has a good visibility from space. Due to the resulting total sensitivity being quite high, nadir viewing satellites provide a valuable additional platform to quantify NO_x production by lightning; strong lightning events over "clean" regions should be clearly detectable in satellite observations. Since the observed enhancement of NO_2 column densities over mesoscale convective systems are lower than expected for current estimates of NO_x production per flash, satellite measurements can in particular constrain the upper bound of lightning NO_x production estimates.

1 Introduction

Lightning NO_x (LNO_x), suggested to be the dominant NO_x source in the tropical upper troposphere (Schumann and Huntrieser, 2007, and references therein), plays an important role in atmospheric chemistry by driving ozone formation and influencing the OH concentration (e.g. Labrador et al., 2005). However, estimates of the total annual NO_x release by lightning are still uncertain, and literature results differ significantly, though they seem to be converging on the range of 2–8 Tg [N] per year (Schumann and Huntrieser, 2007).

Satellite observations using nadir viewing spectrometers, like the Global Ozone Monitoring Experiment (GOME 1&2), the SCanning Imaging Absorption Spectrometer for Atmospheric CHartographY (SCIAMACHY), or the Ozone Monitoring Instrument (OMI) (e.g. Burrows et al., 1999; Bovensmann et al., 1999; Levelt et al., 2006), that provide column measurements of NO_2 on a global scale, allow a new approach to estimate LNO_x production. Some studies have compared mean observed NO_2 columns with lightning measurements (Beirle et al., 2004), flash rates parameterized from cloud top height (Boersma et al., 2005), or modelled LNO_x distributions (Martin et al., 2007). Since lightning activity is highest over tropical land masses, and has its peak in the late afternoon, while current satellite instruments measure in the morning (GOME 1&2, SCIAMACHY) or shortly after noon (OMI), these comparisons mainly detect aged LNO_x. Hence, for quantification of LNO_x production, its lifetime has to be considered, which is also rather uncertain and strongly depending on altitude.

As an alternative to the approaches discussed above, it is also possible to study freshly produced LNO_x directly over individual active thunderstorms occurring at satellite overpass. Within the long time series of satellite measurements with global coverage, several coincidences of lightning activity during satellite overpass are found, mostly over ocean, where the diurnal cycle of flash activity is much smoother than over land, having the positive side effect that interference of other NO_x sources is generally smaller. A prominent example has been described in Beirle et al. (2006). This new approach, which is investigated quantitatively in this study, has the advantage that chemical loss and dilution are negligible (with respect to temporal scales of some hours and spatial scales of typical current satellite footprints, i.e. hundreds to thousands of km^2). Hence, the increase in NO_x can directly be related to flash numbers, e.g., those from the World Wide Lightning Location Network (WWLLN) that are available continuously on global scale (Rodger et al., 2006).

The direct observation and quantification of LNO_x over thunderstorms, however, is strongly affected by the presence of clouds. Generally, clouds shield trace gases below them from the satellite's view. On the other hand, clouds also increase the sensitivity for trace gases at the cloud top or above, due to multiple scattering and their high albedo, respectively. In addition, in the case of NO_x, clouds also affect photolysis, i.e. the partitioning of NO_x into NO and NO_2, while only the latter is detectable in satellite spectra. For quantitative estimates of these effects, radiative transfer modelling is needed.

Here we analyse the sensitivity of satellite observations for detecting LNO_x under thunderstorm conditions. A cloud resolving model, accounting for dynamics and (photo-) chemistry, is used in combination with a Monte Carlo Radiative Transfer Model (RTM) to calculate synthetic satellite observations. Hence the satellite response to the LNO_x which is actually produced can be quantified.

2 Methods

Satellite measurements of tropospheric trace gases, in particular of NO_2, have been used to estimate and constrain emissions in several studies. In most of these studies, clouded observations are simply skipped, as clouds shield the boundary layer from the satellites' view. If one is interested in the observation of freshly produced LNO_x, however, skipping clouded pixels is not possible. Instead, one has to deal with the complications due to clouds.

From spectral satellite measurements, slant column densities (SCDs), i.e., concentrations integrated along the light paths, of NO_2 can be derived. For quantitative interpretations, however, vertical column densities (VCDs), i.e., vertically integrated concentrations, of NO_x are needed that can be directly related to emissions if loss due to chemistry and transport is small.

In Sect. 2.1, we derive a formalism to relate (excess) NO_2 SCDs to (lightning) NO_x VCDs, considering the specific conditions for lightning NO_x. The ratio of NO_2 SCD and NO_x VCD is denoted as "sensitivity" in this study and depends on the profiles of NO_x and NO_2, that are taken from a cloud resolving model (Sect. 2.2), as well as on box-AMFs (Air Mass Factors), that are calculated with an RTM (Sect. 2.3) using the modelled cloud profiles. In Sect. 2.4, the final calculation of sensitivities and "synthetic" NO_2 SCDs for the temporal and spatial range covered by the model is described.

2.1 Sensitivity of satellite observations for NO_x

From UV-vis satellite measurements, slant column densities (SCDs), i.e., concentrations integrated along the light paths, can be derived for various trace gases (e.g., Wagner et al., 2008). For a quantitative interpretation, the SCD S has to be converted into the vertical column density (VCD) V, that represents the vertically integrated concentration. The ratio S/V is given by the air mass factor (AMF) A:

$$S = V \cdot A \tag{1}$$

The AMF reflects the sensitivity of the observation for the investigated trace gas, and depends on various parameters like solar zenith angle (SZA), ground albedo, aerosols and clouds. In particular, due to atmospheric scattering, the sensitivity is a function of altitude, determined by the actual profile of scattering particles/molecules. Hence the total AMF depends on the trace gas profile. One possibility to account for this height dependence is the concept of "box-AMFs" a_i (see Wagner et al., 2007), giving the AMF for a trace gas in layer i. The total AMF can then be expressed as the sum of the box-AMFs a_i, weighted by the normalized profile p_i:

$$S = V \cdot \sum_i p_i \cdot a_i \qquad (2)$$

where i is the vertical layer index, and p_i is the partial trace gas column in layer i, normalized according to

$$\sum_i p_i = 1 \qquad (3)$$

Note that the partial columns are proportional to concentrations for equidistant layers.

In the case of NO_x, in contrast to other trace gases, additional complications arise from the fact that only NO_2, but not NO, is detectable in the UV/vis spectral range. For a given VCD of NO_x ($\mathbf{V}^{NO_x}$), the measured SCD of NO_2 ($\mathbf{S}^{NO_2}$) would be

$$S^{NO_2} = V^{NO_x} \cdot \sum_i p_i \cdot a_i \cdot l_i, \qquad (4)$$

where p_i is still the normalized **NO_x** profile and

$$l_i := \frac{[NO_2]_i}{[NO_x]_i} \qquad (5)$$

is the NO_x partitioning in layer i.

If the product of the box-AMF and the partitioning is defined as

$$e_i := a_i \cdot l_i, \qquad (6)$$

it follows from Eq. (4) that

$$S^{NO_2} = V^{NO_x} \cdot \sum_i p_i \cdot e_i, \qquad (7)$$

and, with

$$E = \sum_i p_i \cdot e_i, \tag{8}$$

follows

$$S^{NO_2} = V^{NO_x} \cdot E \tag{9}$$

in analogy to Eq. (1).

Hence, e_i can be interpreted as the "effective box-AMF" for **NO**$_x$, and is called "visibility" hereafter. The overall conversion factor E is referred to as the "sensitivity". In this study, E will be calculated for conditions in and around cumulonimbus clouds, using NO_x and NO_2 profiles from a cloud resolving model (2.2) and box-AMFs modelled for the respective cloud profiles (2.3). Knowing E, "synthetic" slant columns of NO_2 can be calculated from model profiles of NO_2 and NO_x, simulating satellite measurements. The other way around, observed S^{NO_2} derived from satellite observations can be converted into V^{NO_x}, i.e. satellite NO_2 SCDs can be related to the actual NO_x column via E.

Please note that a two-step conversion (first from NO_2 SCDs into NO_2 VCDs using an overall AMF, and then from NO_2 VCDs into NO_x VCDs using a mean NO_2/NO_x ratio) is not appropriate, since both the box-AMFs and the NO_x partitioning are height dependent, and they do not vary independently because both are particularly influenced by clouds.

In this study, we are interested in NO_x produced by lightning (LNO_x). The LNO_x VCD can be defined by

$$V^{LNO_x} = V^{NO_x} - V^0, \tag{10}$$

with V^0 being the appropriate "background" NO_x VCD (including the stratosphere), i.e. the column one would observe in absence of lightning.

Similarly, we define the S^{NO_2} excess as

$$\Delta S^{NO_2} = S^{NO_2} - S^0. \tag{11}$$

Note that, in practise, the subtraction of the background column S^0 removes the tropospheric background and the stratospheric part of the column, but also accounts for uncertainties in the absolute calibration of SCDs (see e.g. Wenig et al., 2004).

In general, ΔS^{NO2} is *not* just a response to the produced LNO_x (and, hence, is *not* denoted as S^{LNO_2} in Eq. 11), since cumulonimbus clouds and convection also affect the visibilities and profiles, respectively, of background NO_x. In particular, background NO_x in the lower troposphere is shielded effectively by high, optically thick clouds.

In analogy to Eq. (9), we define S^{LNO_2} as

$$S^{LNO_2} = V^{LNO_x} \cdot E^L \tag{12}$$

with

$$E^L = \sum_i p_i^L \cdot e_i^L, \tag{13}$$

i.e. using profiles of LNO_x (background corrected) and visibilities calculated for the actual (possibly clouded) viewing conditions. In the following, the letter "E" refers to sensitivities of lightning NO_x, even if the superscript ^{L} is omitted.

In this study, we calculate sensitivities for LNO_x using Eq. (13) and derive synthetic SCDs of LNO_2 by Eq. (12). In the appendix, a relationship between ΔS^{NO_2} and S^{LNO_2} is derived. It is shown that S^{LNO_2} can actually be approximated by ΔS^{NO_2} (i.e., the actual response to lightning NO_x that a satellite would detect), if the tropospheric background levels of NO_x are negligible. The results of our study are hence limited to cases of lightning events over rather clean regions; however, in cases in which a significant fraction of NO_x originates from other sources, the discrimination and quantification of LNO_x is difficult in any case, also by other methods.

In Beirle et al. (2006), an approach analogous to Eq. (12) was applied for the transformation of S^{LNO_2} into V^{LNO_x}, using literature values for the NO_x profile (Pickering et al., 1998; Fehr et al., 2004) and partitioning (Ridley et al., 1996) as well as for the box-AMFs (Hild et al., 2002) under cumulonimbus cloud conditions. The resulting conversion factor (defined in Beirle et al., 2006, as V^{LNO_x}/S^{LNO_2}, i.e. the inverse of E in Eq. 12) of 4.0 (2.1–7.1) corresponds to E=0.25 (0.14–0.48). It has to be noted, however, that this sensitivity was calculated from profiles p_i, l_i, and a_i that (a) are averages, i.e. do not reflect the high variability of meteorological and (photo-) chemical conditions within a mesoscale convective system (MCS), and (b) have been taken from different literature sources and for different thunderstorms, thus are inevitably inconsistent with respect to meteorological/chemical conditions, in particular trace gas profiles, cloud top height and -thickness.

Here we use a cloud resolving model, described in Sect. 2.2, in combination with a Monte-Carlo radiative transfer model (see Sect. 2.3) to: (a) calculate box-AMFs a_i for thunderstorm simulations, (b) calculate sensitivities E and hence (c) derive S^{LNO_2} (i.e., synthetic satellite measurements) for a variety of thunderstorm scenarios consistently (Sect. 2.4).

2.2 Cloud resolving modelling: CSRMC

The cloud system resolving model including chemistry (CSRMC) is based on a prototype version of the Weather Research and Forecasting (WRF) model (Skamarock et al., 2001) and is described in detail in Salzmann et al. (2008). It includes a simple flash rate parameterization based on Price and Rind (1992) which is tuned to approximately reproduce observed flash numbers in the TOGA COARE/CEPEX region. The partitioning between intra-cloud (IC) and cloud-to-ground (CG) flash rates is diagnosed using an empirical relationship (Price and Rind, 1993) between $Z=N_{IC}/N_{CG}$ and the cold cloud height (defined as the vertical distance between the 0°C isotherm and cloud top). In the present study, results from the LTN3D run of Salzmann et al. (2008) are analyzed, in which Z=10.43. The vertical distributions of IC and CG flashes follow DeCaria et al. (2000, 2005), i.e. CG flash segments are assumed to have a Gaussian distribution and IC segments are assumed to have a bimodal distribution corresponding to a superposition of two Gaussian distributions. CG and IC flashes are assumed to produce 10×10^{25} and 5×10^{25} NO molecules per flash, respectively. Flash rates and lightning NO production are calculated separately for each updraft core and for each anvil. Cores and anvils are identified as described in Salzmann et al. (2008). CG flashes are horizontally placed at the location of the maximum vertical updraft, which could lead to an over-estimate of NO_x transported to the upper troposphere (see the discussion in Sect. 4.1 below).

A "background" CH_4-CO-HO_x-NO_x tropospheric chemistry mechanism with additional reactions involving PAN (peroxy acetyl nitrate, $CH_3C(O)O_2NO_2$), and loss reactions of acetone (CH_3COCH_3) which is based on the mechanism from MATCH-MPIC (von Kuhlmann et al., 2003) has been used for simulating the influences of deep convection and lightning on chemistry in the TOGA COARE/CEPEX region.

2.3 Radiative transfer modelling: The Monte-Carlo Model McArtim

The Monte Carlo (MC) radiative transfer model (RTM) McArtim was developed in the satellite group Mainz/Heidelberg in recent years (Deutschmann, 2008; see McArtim documentation on http://joseba.mpch-mainz.mpg.de/matr/tracy_II/documentation/McArtim_Documentation.html). It is an advancement of the RTM TRACY-II (Deutschmann and Wagner, 2006) that has been validated in a comparison study involving several RTM codes (Wagner et al., 2007).

MC is a well suited approach to model radiative transfer, in particular for a cloudy atmosphere. For given atmospheric conditions, i.e. profiles of temperature, pressure, and optical extinction coefficients from clouds and/or aerosols, McArtim generates a light path ensemble in a backward Monte-Carlo mode (Marchuk et al., 1980). From the resulting light path ensemble, in addition to radiances also box-AMFs can be derived (Wagner et al., 2007; Deutschmann, 2008) that are evaluated in this study.

2.4 Sensitivities and synthetic satellite SCDs for the TOGA-COARE lightning simulation

The CSRMC run in Salzmann et al. (2008) spans one week of a 3-D simulation of meteorology and (photo-) chemistry for thunderstorms in the Pacific, with output every 30 min, and covers an area of 278×278 km^2 with 2 km spatial resolution in the horizontal and 500 m in the vertical. In this study, we consider the profiles from ground to 20 km altitude. In the following, we use the term "output time-step" (OTS) to denote the entity of data at a given output time-step, whereas "scene" denotes the entity of profiles and columns for a single 2×2 km^2 pixel.

For our analysis, we skip the night-time output time-steps (no photochemistry), and remove 10 pixels on each side in order to avoid boundary effects (instead of 8 pixels as in Salzmann et al., 2008). This leaves 138 OTSs with 119×119 pixels of 2×2 km^2 each, in total about 2 million scenes. For each of these scenes, a synthetic satellite observation is calculated:

First, the hydrometeor mixing ratios from the cloud resolving model are used to calculate visible extinction coefficients. Here we use the parameterization given in Platt (1997) (see page 2090, Eq. 28 therein):

$$\sigma = \mathrm{j} \cdot \mathrm{W}^{\mathrm{k}} \tag{14}$$

where W is the ice/water content, σ is the extinction coefficient, and experimental values for the parameters j and k are given in Table 8 in Platt (1997) as 9.27 and 0.68, respectively. This parameterization has the significant advantage that it directly relates the liquid water content to the extinction coefficient, without the need of an effective radius. The resulting cloud optical thickness (COT) reaches about 120 at its maximum. Note that the experimental values in Platt (1997) are given for cirrus and frontal ice clouds. However, the resulting COTs are reasonable. In addition, our results are robust with respect to modifications of the extinction coefficients (see Sect. 4.1).

Second, the extinction coefficients are fed into the MC-RTM McArtim to calculate box-AMFs a_i for the respective scene, assuming horizontally homogenous clouds, and assuming that the scene is not affected by neighbouring scenes (independent pixel approximation, IPA).

The RTM is run assuming the cloud droplets having a single scattering albedo of 1 and a Henyey-Greenstein phase function with an asymmetry parameter of 0.85. Ground albedo was set to 5%, and calculations are performed for a solar zenith angle (SZA) of 20°. The wavelength is set to 440 nm, matching the spectral fitting window of NO_2 retrievals.

Third, tropospheric VCDs of LNO_x are estimated: For this, the remaining stratospheric (<20 km) as well as the tropospheric background NO_x columns have to be removed. This is done by subtracting a reference NO_x profile that is estimated as the mean of the 1416 scenes (1% of all scenes per OTS) with the lowest NO_x VCD for each OTS. The estimated background columns (i.e. the integrated reference NO_x profiles) range from 2.5–3.8×10^{14} moelc/cm^2. From the background corrected NO_x profiles, background corrected NO_2 profiles are calculated using the actual NO_2/NO_x ratio for each layer. Hereafter, all NO_x/NO_2 profiles/columns are corrected for this background. These corrected profiles/columns contain the lightning produced NO_x/NO_2, and are thus denoted as LNO_x/LNO_2 in the following.

Finally, visibilities e_i (Eq. 6) and sensitivities E (Eq. 13) are calculated, using the NO_2/NO_x ratio (l_i) from the CSRMC and the RTM box-AMFs (a_i). The synthetic SCDs of LNO_2 are calculated according to Eq. (12).

3 Results

For 2 million scenes from the CSRMC model run, box-AMFs and sensitivities are calculated. For the further analysis, we only consider (a) output time steps (OTSs) with more than 50 flashes, resulting in 50 OTSs, and for each of these OTS (b) scenes with $V^{LNO_x}>10^{14}$ molec/cm^2, to restrict our study to cases that actually contain LNO_x (see Appendix A, Eq. A4), resulting in 167820 scenes. For the calculation of spatial means, however, all scenes are considered (see below). Please recall that in the following (if not labelled differently), “sensitivity” and “E” refer to the sensitivity for lightning NO_x according to (Eqs. 12 and 13), even if the superscript ^{L} is omitted.

Figure 1 shows the LNO_x profile, the respective NO_x partitioning l_i, the box-AMFs a_i, and the visibility e_i, for two selected, illustrative sample scenes.

The first selected example (orange) shows a typical “C-shape” LNO_x profile (a) with a pronounced peak at ~15 km and almost no NO_x in the middle troposphere. The NO_x at the ground (b) is nearly completely present as NO_2, while at 15 km it is dominated by NO due to the high actinic flux and the low temperatures. The box-AMFs (c) above 10 km are slightly higher than 2, similar to the stratospheric AMF, but jump to a value of 4 at 9 km due to an optically thick cloud (COT=41.5). Below, a_i decreases, and reaches values <0.1 for altitudes <4 km and <0.02 for the lowest layer. The box-AMF profile is generally similar to the box-AMF presented in Hild et al. (2002). The resulting visibility is low (0.02) at the ground (due to the low a_i), peaks at 8 km, reaching ~0.9, and is low (min. 0.06) again in the UT due to the low NO_2/NO_x ratio. The resulting sensitivity is rather low (E=0.11), since the LNO_x is C-shaped, i.e., has its peaks where the visibility is small.

The second example (red) displays a case of a very high LNO_x column shortly after the release of fresh NO from lightning: the NO_2/NO_x (b) at the ground has not yet reached photo stationary state. The LNO_x concentration (a) shows no C-shape, but instead is high throughout the troposphere, peaking at 8 km. The box-AMFs (c) result from a very high (CTH=17.8 km, where Cloud Top Height is defined as the highest altitude where hydrometeor mass mixing ratios exceed 0.01 g/kg), optically thick (COT=80.5) cumulonimbus cloud. As in the first example, the visibility is low at the ground as well as at the tropopause, but peaks at 13 km (i.e., 2 km below the peak in box-AMFs). As a result of the high LNO_x throughout the troposphere, the resulting sensitivity is much higher (E=0.50) than in the first case.

After discussing these two selected examples that illustrate some general features of p_i, l_i, a_i, and e_i, we now analyse mean conditions over the complete simulated data. To investigate possible systematic differences, the scenes have been grouped into five regimes that are defined as follows (the listed colours are used in all following plots to identify the regimes):

- Regime I (light blue): defined by COT<1.
- Regime II (blue): defined by 1<COT<10.
- Regime III (green): defined by 10<COT<30.
- Regime IV (orange): defined by 30<COT<50.
- Regime V (red): defined by 50<COT.

This classification serves as indicator of the different regimes of a deep convective system: Regime I summarizes cloud free conditions. The outflow will mostly fall in Regime II, whereas anvils will be classified as Regime III or IV. The cores are predominantly classified as Regime V due to the high COT.

Note that we also applied a finer classification, using vertical wind speeds to separate up- and downdraft regions. However, we found no systematic differences in the sensitivities for scenes with up- or downdraft conditions (the correlation coefficient of sensitivities E and vertical wind speeds w is $R=-0.06$), and thus classify the regimes simply by COT in this study.

Figure 2 shows the mean profiles for the different regimes. The general features are similar to the examples shown in Fig. 1, but reveal some systematic differences for the five regimes: The $\mathrm{LNO_x}$ concentrations (a) show a peak at the ground and at the tropopause (note the change in scale by a factor of 10 compared to Fig. 1a); however, the profiles of Regimes I&II have low values in the middle troposphere, whereas the concentration is high throughout the troposphere for Regime V. The $\mathrm{NO_x}$ partitioning (b) is close to 1 at the ground (but only 0.7 for cloud free scenes due to the higher photolysis) and decreases to ~0.05 at 15 km. The box-AMFs (c) are low at the ground, peaking in the upper troposphere (except cloud free), reaching values up to 4 for Regime V, and approaching stratospheric box-AMFs at the tropopause. It has to be noted that the smoothness of the box-AMFs is a result of the averaging process, while individual scenes show sharp discontinuities at the cloud top (compare Fig. 1c). The resulting visibility (d) again shows the “inversed C-shape”, peaking in the middle troposphere and having low values at the ground as well as at the tropopause. For Regimes I and II (i.e. COT<10), visibility at the ground is still quite substantial (∼0.5). Note that box-AMFs differ significantly for the five regimes, increasing from 2 (I) to 4 (V) at about 10 km, and decreasing from 1 (I) to almost 0 (V) at the ground. The visibilities, on the other hand, vary much less from regime to regime.

The resulting mean sensitivities are also similar for the five regimes and range from 0.44 (Regimes I and II) over 0.41 (Regime III) to 0.53 (Regimes IV and V). Thus, scenes of medium COT, as occurring in the anvil, show the lowest sensitivity, whereas E is higher both for Regimes I and II (due to the “transparency” of the cloud) and for Regimes IV and V (due to the rather smooth LNO_x profile that is high throughout the troposphere, and the higher box-AMFs).

To also illustrate the extremes of the simulated profiles within each regime, Figs. 3 and 4 show the scenes of lowest and highest sensitivity for the five regimes, respectively (for these plots, we ignored scenes where the background-corrected profiles of NO_x become negative).

Figures 3a and 4a in particular illustrate the high variability of LNO_x profiles. The resulting visibilities (Figs. 3d and 4d), however, all show the same general pattern of a minimum at the tropopause, a maximum in the free troposphere between 5 and 10 km (except for being ∼13 km for Regime IV in 4d), and a second minimum at the ground.

As a consequence, highest sensitivities (Fig. 3) are generally found for LNO_x profiles with a substantial fraction in the middle troposphere, where visibility is highest and can reach values of up to 3 for Regime V. Cases of lowest sensitivity (Fig. 4), on the other hand, generally show no LNO_x between 5 and 10 km. The minimum scene of regime IV is exceptional in this case: Here we have fresh lightning production (note that only 50% of the NO_x is NO_2 at the ground!) that is shielded by a high cloud (CTH=17.3 km). Thus, low sensitivities occur for LNO_x below or above the cloud, while high sensitivities are observed for LNO_x within the cloud.

These extreme cases illustrate under which conditions LNO_x is highly visible or almost invisible for nadir viewing satellites. However, these events are very rare in the complete simulation. The resulting sensitivity of all scenes has a mean of 0.41, a median of 0.39, and a standard deviation of 0.15. Figure 5 displays the frequency distribution of the modelled sensitivities. Hence, despite the high variability of meteorological and chemical conditions within the thunderstorm simulation, the resulting sensitivities vary less than we had initially anticipated. Figure 6 shows a scatterplot of the sensitivity against the respective COT for all considered scenes. The correlation coefficient is $R=-0.27$. If sensitivities are averaged for the different regimes separately, we find means of 0.45, 0.42, 0.28, 0.32, and 0.40 for Regimes I–V, respectively. Note that these mean sensitivities differ from the numbers given in Fig. 2, since here we directly give the average of the individual sensitivities, while in Fig. 2 the "mean" sensitivities are calculated from the averaged profiles, partitioning, and box-AMFs. As in Fig. 2, but more obvious, scenes with medium COT (Regime III) have the lowest sensitivity. Note that the sensitivities show no significant dependency on $VLNO_x$ ($R=-0.17$).

Besides discussing typical, mean, and extreme profiles, the model data also allows us to study the spatial patterns of the resulting V^{LNO_x} and S^{LNO_2} columns and the respective sensitivities at a given OTS. Figure 7 displays the spatial distribution of COT and regime classification for two selected OTSs that have low and high overall sensitivity. The left column displays the OTS from 19 December 1992, at 22:30 UTC. This is an early stage of the simulation. In the northern part, a strong, quite homogenous convective system can be seen. In the right column, from 23 December 1992, 21:30 UTC, the situation is much less homogenous. There are several convective cells distributed over the model domain. The respective model flash counts within the last 30 min are 304 and 83.

Figure 8 displays maps of V^{LNO_x}, S^{LNO_2}, and E, for the respective OTS. In both cases, the resulting sensitivities show spatial structures that relate to Fig. 7. Again, a tendency towards lower sensitivities for Regime III is noted. However, the differences between the mean sensitivities for the different Regimes are much smaller than the spatial variability seen in Fig. 8. Thus the resulting spatial patterns of E are mainly a consequence of some horizontally smooth patterns for p_i, l_i, and a_i, and can only partly be summarized by a simple dependency on regime classification, i.e., on COT.

In practice, a quantitative estimate of (L)NO$_x$ using satellite measurements is typically based on a spatial mean, rather than on single columns, to account for uncertainties in flash locations and transport. We calculate the spatial mean sensitivity for each OTS (denoted as E_{total} hereafter) as

$$E_{total} = \frac{\overline{S^{LNO_2}}}{\overline{V^{LNO_x}}} \tag{15}$$

i.e. the spatially mean enhancement in the synthetic satellite observation in relation to the spatially mean release of LNO$_x$. Note that a spatial mean eliminates individual scenes of extreme high/low sensitivity if they contain no (or low) lightning NO$_x$. It is the aim of this study to provide the total sensitivity (Eq. 15) for use in future observational studies, where the produced LNO$_x$ can be estimated from measurements of mean (background corrected) SCDs of NO$_2$, by applying E_{total}.

The resulting sensitivities E_{total} for the sample OTS are 0.31 and 0.66, respectively. The averaging of the total mean sensitivities over all OTSs results in E_{total}=0.46 (standard deviation 0.09). This is slightly higher than the mean of the individual sensitivities due to nonlinearities (Eq. 15) and due to the fact that scenes with $V^{LNO_x}<10^{14}$ molec/cm^2 are skipped in the average of individual sensitivities, but not in the calculation of E_{total}.

The S^{LNO_2} shown in Fig. 8b is the synthetic slant column, i.e. the column a nadir viewing satellite (with 2×2 km^2 spatial resolution) would actually "see". Note the high spatial gradients: due to the local release of high amounts of LNO$_x$, individual pixels show $S^{LNO_2}>5\times10^{15}$ above the background. Hence, studies of freshly produced LNO$_x$ from space will profit from improved spatial resolutions of future satellite instruments.

Current instruments have a coarser spatial resolution, e.g. 30×30 km^2 for SCIAMACHY in short integration time mode. Figure 9 shows the synthetic S^{LNO_2} for this SCIAMACHY resolution, illustrating the loss of spatial information. Note that average S^{LNO_2} are calculated as the mean of the pixels (2×2 km^2) within the 30×30 km^2 weighted by the respective intensities (clouded pixels are brighter and hence contribute more light to the detector measurement), as in real satellite observations. Total sensitivities are 0.31 and 0.71, i.e. for the second example slightly higher than for the original model resolution. The increase is mainly caused by the two pixels with high sensitivity (Fig. 9c) that result from the intensity weighted average of S^{LNO_2}. At this OTS, a small region with high S^{LNO_2} dominates the 30×30 km^2 pixel since it coincides with high COT. Note, however, that in general S^{LNO_2} does not correlate with COT (R=0.07). So the principal results of our study on mean sensitivities are not affected by the footprint of the satellite instrument. However, the loss of spatial information is evident.

4 Discussion

4.1 Uncertainties

The presented calculation of synthetic satellite measurements and sensitivities is based on model profiles of NO_x, NO_2, and clouds, combined with radiative transfer calculations. Here we discuss the uncertainties due to the assumptions made and methods applied in this study.

4.1.1 Uncertainties of the model

Cloud system resolving models (CSRMs) can explicitly resolve an important part of the cloud system dynamics, while cloud microphysical processes are parameterized. The present model is the first of its kind in that it includes chemistry in a cloud system resolving model framework in which so-called large scale forcing terms are added to the equation for water vapour and temperature, thus largely constraining the simulations to reproduce the observed total precipitation.

The meteorological setup applied in the present study has been evaluated in Salzmann et al. (2004, 2008) based on observations in the TOGA COARE campaign (Webster and Lukas, 1992), suggesting that the model performance is comparable to that found in other TOGA COARE CSRM studies. The chemistry part of the CSRMC has been extensively evaluated in Salzmann et al. (2008) based on observations from adjacent regions, showing reasonably good agreement for key compounds (see electronic supplement to Salzmann et al., 2008, http://www.atmos-chem-phys.net/8/2741/2008/acp-8-2741-2008-supplement.pdf, for details).

We have tuned the lightning parameterisation to approximately yield observed flash numbers in the TOGA COARE/CEPEX region. Large uncertainty exists, however, with respect to the IC/CG ratio, which can not be inferred with confidence from the lightning observations during TOGA COARE. The simulated IC/CG ratio (10.43) is in line with observations of average tropical IC/CG ratios by Pierce et al. (1970). The horizontal and vertical placement of IC and CG flashes introduces an additional uncertainty. CG flashes are horizontally placed at the location of the maximum vertical velocity. This choice is consistent with Ray et al. (1987), who found, based on dual Doppler radar and very high frequency lightning observations, that in a multi-cell storm, lightning tended to coincide with the reflectivity and updraft core. It could, nevertheless, potentially lead to a small over-estimate of the upward transport of lightning NO_x.

While the vertical placement is based on observations of lightning channel segments as in DeCaria et al. (2000) (see above), we do not explicitly take into account branching for placing flashes horizontally. This could result in an overestimate of local NO maxima. On the other hand, the flash rates and NO production are calculated for each 8 s model time step, which introduces some artificial “smearing out” and a reduction of the local NO maxima. Finally, the simulated NO/NO_2 ratios depend on the number of NO molecules produced per flash, which is still rather uncertain. This effect is difficult to quantify, since multi-day 3-D sensitivity studies including chemistry are still computationally expensive.

It has to be noted, however, that the modelled sensitivities (including scenes with IC as well as CG flashes) show low variability over all scenes; 81% of all sensitivities are between 0.2 and 0.6. In addition, if we shift the NO_x and NO_2 profiles vertically by one layer (500 m) either up or down, our results change by less than 5%. Hence the impact of a possible systematic LNO_x profile bias on our results is likely to be small.

4.1.2 Uncertainties of the radiative transfer calculations

The Monte Carlo RTM McArtim, successor of TRACY-2, is a powerful, flexible program for the calculation of box-AMFs under various atmospheric conditions. The resulting radiances and box-AMFs have been validated (Wagner et al., 2007). At present, however, only 1-D cloud profiles can be considered. Future versions of McArtim will allow the definition of 3-D fields of scattering particles (Tim Deutschmann, personal communication).

We calculated box-AMFs using the independent pixel approximation (IPA). RTM is applied for 1-D cloud layers for each pixel separately, neglecting the horizontal photon fluxes between neighbouring pixels of different cloud properties. For the rather small pixels of 2×2 km^2 size, the limitations of the IPA may become an issue (Marchak et al., 1998). For instance, for the extreme case of a clouded scene with high COT surrounded by cloud free scenes, the cloud would scatter the sunlight out of the considered pixel, whereas in our calculation, assuming homogenous cloud layers, light also comes back from the surrounding pixels. Hence, a 3-D calculation would lead to a more effective shielding than in our analysis, and we overestimate the visibility below the cloud for such an extreme case. On the other hand, a cloud free pixel within clouded pixels would be influenced by stray light coming from the surrounding pixels, that increases the visibility at the altitudes of the surrounding clouds. Hence, in such cases we underestimate the actual visibility. Things get even more complicated due to the slant irradiation (here: SZA=20°), which leads to shadowing effects and irradiation of the cloud flanks.

A quantification of these effects is rather difficult. The hydrometeor as well as the NO_x profiles differ from pixel to pixel. Currently, 3-D clouds are not yet implemented in McArtim, and the computational effort of a full 3-D run over the complete model period would exceed the available computer power. Furthermore, photolysis rates calculated in the CSRMC also use the IPA and cannot be modified afterwards.

So the IPA may lead to a bias of our results, but its overall impact is probably of minor importance: First, the distribution of hydrometeors and NO_x on the 2*2 km^2 resolution is in general rather smooth. Extreme jumps of COT or NO_x from one pixel to another occur occasionally, but are exceptional. Second, the effects of the IPA can result both in an over- as well as an underestimation of visibilities, that at least partly cancel out each other. Finally, the change in photon paths for a real 3-D run would change the box-AMFs, as well as the photolysis rates, damping the net effect (in other words: more light through the cloud increases the box-AMF a_i (enhancing visibilities e_i), but decreases the NO_2/NO_x ratio l_i (decreasing visibilities e_i), and vice versa).

For the RTM runs, the following assumptions on viewing geometry and optical cloud properties have been made: solar zenith angle (SZA)=20°, single scattering albedo (SSA)=1, asymmetry parameter g=0.85, ground albedo=5%, and extinction coefficients according to Eq. (14). To study the impact of these settings, we modified all parameters exemplarily for the first sample OTS with E_{total}=0.31. Table 1 lists the modifications made and the resulting absolute and relative change in E_{total}.

The sign of the changes are as expected: Higher SZA mainly has an impact on the cloud free scenes, increasing the light paths, and hence the visibility for the free troposphere. Absorbing properties of the cloud droplets (SSA<1) lead to lower AMFs below the clouds due to more effective shielding, and thus lower sensitivity. If the scattering would be more/less diffusive (g=0.8/0.9), generally less/more photons will penetrate the clouds “forth and back”. A lower/higher ground albedo decreases/increases the visibility of the lower layers.

The relative change in sensitivity, however, is rather small for all cases. Hence, none of the assumptions is critical for our conclusions. The parameterization of extinction from the modelled hydrometeors (Eq. 14); see Platt, 1997) is not critical, either. A doubling/halving of the extinction coefficients results in optically thicker/thinner clouds and hence more/less effective shielding, i.e. lower/higher sensitivities. The relative changes are significant (−13% and +19%, respectively), but still rather moderate.

4.1.3 Uncertainties of the calculation of synthetic slant columns and sensitivities

For the calculation of sensitivities according to Eq. (15), the model profiles have to be corrected with respect to the “clean” background columns. These backgrounds have to be estimated from the model run itself. Taking the 1% “cleanest” scenes is a good working solution for the estimation of background NO_x. This background estimate is rather conservative to avoid negative concentrations. As a consequence, large regions of the simulated OTS that should be “clean” still show VCDs of some 10^{13} molec/cm^2 of LNO_x (compare Fig. 8). For our analysis of individual sensitivities per scene, the impact of a possible background bias is minimized by the applied threshold of 10^{14} molec/cm^2 for LNO_x. For the calculation of E_{total}, the impact of background is also rather small, since the integrated column densities are dominated by scenes with high columns. In addition, the difference of the sensitivities for background- and for lightning NO_x is rather small for cloud free scenes.

For the background correction of NO_2 profiles, we subtract the background NO_x from the total NO_x profile, and split the corrected NO_x profile to NO and NO_2 according to the original model partitioning (note that we can *not* simply subtract the background NO_2 profiles that are valid for cloud free scenes only!). I.e., we assume that the background NO_x, that would be present if there would not have been any LNO_x production, would have the same partitioning as the actual model total NO_x. This approach neglects possible nonlinearities of the photochemistry due to additional LNO_x; however, for scenes where LNO_x is much higher than the background, the latter is irrelevant anyway. On the other hand, if LNO_x is low, it should not affect the NO_x partitioning of the background.

In Appendix A, it is shown and discussed that the NO_2 excess ΔS^{NO_2} for uncorrected profiles can be decreased and even become negative, if the shielding effect of the clouds for background NO_x overcompensates the column increase due to lightning NO_x. In Fig. 10, we hence plot also V^{NO_x}, S^{NO_2}, and sensitivities for the original, uncorrected profiles. In (b) it can clearly be seen that for some regions of the OTS (generally speaking: where COT is high, but LNO_x is low) the SCDs of NO_2 are actually lower than the background. For these regions, the second term of Eq. (A3) is obviously not negligible. For relatively high background levels, LNO_2 is thus likely to be "overseen" from space. Hence, the quantification of LNO_x using satellite observations only has good prospects for events with high flash rates and low background NO_x.

In our study, we ignore the shielding of background NO_x. The resulting sensitivities are thus slightly biased for the thunderstorms under investigation, but should be appropriate for stronger thunderstorms with higher flash rates, which should be selected for quantitative studies, where background NO_x can indeed be neglected.

4.1.4 Representativeness

In this study, a number of simulated mesoscale convective systems (MCSs) and isolated storms have been investigated in the TOGA COARE/CEPEX region over several days. During the simulation, different stages of MCS evolution are captured. Hence our study comprises the high spatial and temporal variabilities of convective systems.

The TOGA COARE/CEPEX region is located in the Pacific Warm Pool, where deep convection is very frequent, with an annual maximum in January/February. Especially during the seven day episode from 19–26 December 1992, relatively high flash rates have been simulated due to frequent deep convection associated with the onset of a westerly phase of the Intra-Seasonal Oscillation (e.g. Salzmann et al., 2004). The simulated peak flash rates per storm are nevertheless at least an order of magnitude below those observed during vigorous continental thunderstorms. However, tropical marine convective systems are the first choice for studies of fresh LNO_x, since the background NO_x is generally lower, and the diurnal cycle of flash activity is less dominated by late afternoon as for continental lightning, i.e. more occurrences during the currently available satellite overpasses can be found.

The simulated mesoscale convective systems and individual thunderstorm reflect the general features of tropical marine thunderstorm dynamics, (photo-) chemistry, and profiles of hydrometeors and LNO_x. Our results are robust with respect to modifications of RTM settings and even moderate perturbations of the simulated NO_x profiles. Hence our results are likely representative for tropical marine thunderstorms. However, the question remains open, how far estimates of LNO_x production based on tropical marine thunderstorms can be extrapolated to global scale.

Further studies will be required in order to investigate the representativeness of our study, involving additional thunderstorm simulations, probably also with additional cloud resolving- and radiative transfer models.

4.2 Implications

Our study results in a mean total sensitivity of 0.46 for lightning NO_x. The synthetic satellite SCDs of LNO_2 reach values up to 5×10^{15} molec/cm^2 for single 2×2 km^2 pixels. However, for a resolution of 30×30 km^2, maximum S^{LNO_2} is only about 2×10^{14} molec/cm^2 above background. This implies that the LNO_x production of the analyzed thunderstorms probably would not have been visible for an instrument like SCIAMACHY. However, if the retrieved sensitivity of 0.46 is representative for thunderstorms globally, then a number of e.g. 250 flashes within a SCIAMCHY pixel (30×60 km^2) would lead to an enhancement of S^{NO_2} of 10^{15} molec/cm^2, which should be clearly visible from space. (Note that in the WWLLN data for 2004–2006, we found 338 SCIAMACHY pixels with more than 250 flash counts, and 5676 pixels with more than 25 flash counts within the last 60 min prior the satellite overpass. These flash counts have to be scaled up by a factor of more than 5–10, since the WWLLN detection efficiency is about 10–20% around Australia and Indonesia, and far below 5% for South America and Africa (Rodger et al., 2006). For this estimate we assumed a mean LNO_x production of 15×10^{25} molec [NO_x] per flash, as given as best estimate in Schumann and Huntrieser (2007), corresponding to a global LNO_x production of 5 Tg [NO_x] per year. However, previous estimates of LNO_x production using satellite data (Beirle et al., 2004, 2006; Boersma et al., 2005; Martin et al., 2007) generally find lower estimates. Moreover, if we use the resulting sensitivity derived in this study to update the results of Beirle et al., 2006, in which a constant sensitivity of 0.25 was estimated and applied, we estimate a total LNO_x production of only 0.9 (instead of 1.7) Tg per year, or 2.9 (instead of 5.4) $\times 10^{25}$ molec [NO_x] per flash. In addition, preliminary estimates of fresh lightning NO_x from SCIAMACHY measurements over active thunderstorms (as indicated by WWLLN measurements) are much lower than would be expected for an actual release of 15×10^{25} molec [NO_x] per flash. This discrepancy to other studies (Schumann and Huntrieser, 2007, and references therein) might indicate that the global lightning production is currently overestimated. Hence, further studies of fresh LNO_x from satellites could potentially lead to a constraint on the upper bound of total NO_x production by lightning. However, the discrepancies could also indicate systematic differences of the LNO_x release by flashes over tropical land masses in the late afternoon (dominating global lightning activity), compared to flashes over tropical oceans before or shortly after noon (i.e. during the current satellites' local overpass times).

5 Conclusions

For the first time, we investigated the sensitivity of nadir viewing satellite instruments for freshly produced lightning NO_x under conditions simulated in and around cumulonimbus clouds, considering (photo-) chemistry and radiative transfer consistently. From our study, we come to the following conclusions:

1. The box-AMFs a_i for NO_2 in cumulonimbus clouds are close to stratospheric values above the cloud, jump to values up to 5 at the cloud top, and decrease towards the ground, but can still reach values of 1 several km below the cloud top. Below the cloud bottom, a_i is close to zero. These results are similar to those shown in Hild et al. (2002).

2. Since NO_x at the tropopause is almost all present as NO (on average 95% at 15 km), but only NO_2 can be detected in UV-vis spectra, the visibility for NO_x (e_i) is low (0.2) at the cloud top, highest (1–2) in the cloud middle or even at the cloud bottom, and low (0–0.5) below the cloud. This simply means: NO_x below the cloud is shielded, NO_x above the cloud is photolysed, but NO_x inside the cloud can be seen well from space.

3. Individual sensitivities E vary due to the thunderstorm dynamics. Lowest values are found where NO_x peaks below or above the cloud, whereas E is highest for NO_x within the cloud.

4. The overall variability of E in time and space is rather small (given the large variability of thunderstorm dynamics).

5. On average, observations over anvils show the lowest sensitivities.

6. Total (i.e. spatially averaged, Eq. 15) sensitivity is 0.46 (σ=0.09) (mean of all OTSs).

7. Lightning produced LNO_x lead to very high NO_x concentrations within the lightning channel, resulting in extreme horizontal gradients in the NO_x columns. Hence, improved spatial resolution of future nadir UV-vis satellite instruments is not only favourable for studying ground sources, but in particular for LNO_x.

8. Our results are robust with respect to modifications of RTM settings, and even to moderate perturbations to the simulated NO_x profiles.

9. Our results are derived, and only valid, for scenarios of low tropospheric background levels of NO_x. Otherwise, the shielding of boundary layer NO_x can even result in a negative response of the observed NO_2 excess to lightning, and quantitative estimates are not possible.

10. From our results, a satellite measurement with a footprint of e.g. 30×60 km^2 (nominal SCIAMACHY resolution) over a thunderstorm/MCS generating 250 flashes should lead to an increase in the NO_2 SCD of 10^{15} molec/cm^2, assuming a LNO_x production of 15×10^{25} molec [NO_x] per flash, (if outflow can be neglected), i.e., must be observable from space. Preliminary comparisons of satellite observations with flash

counts, however, indicate significantly lower LNO_x production. Hence, future studies of LNO_x using nadir viewing satellite data potentially provide an upper bound for global LNO_x production.

Finally, future studies will be needed to reveal how representative this case study is with respect to global lightning, at least to the extent that this is possible, given the difficulties for regions with non-negligible background levels of NO_x. In this respect, a satellite instrument on a late afternoon orbit, or a geostationary satellite, allowing selected continental thunderstorms with high flash rates at low background (e.g. in the Congo basin) to be studied, would be of particular value.

Appendix A

Impact of background NO_x

In Eq. (12), S^{LNO_2} is calculated from E^L and V^{NO_x}. In a real measurement, the NO_2 excess ΔS^{NO_2} (see Eq. 11), however, is the quantity that can be derived. Here we give a relation of ΔS^{NO_2} and S^{LNO_2}.

Starting from Eq. (11), we find

$$\Delta S^{NO_2} = S^{NO_2} - S^0 = V^{NO_x} \cdot \sum e_i^* \cdot p_i^* - V^0 \cdot \sum e_i^0 \cdot p_i^0 \tag{A1}$$

The asterisk shall indicate that visibilities as well as profiles of the actual scenario might differ from background conditions (labelled by superscript ^{0}), for instance due to clouds.

We now split V^{NO_x} in V^{LNO_x} and V^0 according to Eq. (10):

$$\Delta S^{NO_2} = V^{LNO_x} \cdot \sum e_i^* \cdot p_i^L + V^0 \cdot \sum e_i^* \cdot \tilde{p}_i^0 - V^0 \cdot \sum e_i^0 \cdot p_i^0 \tag{A2}$$

Note that the profile of the background NO_x can also be modified (due to convection). The modified profile of background NO_x is indicated by the tilde.

The first summand is identical with S^{LNO_2} (see Eq. 12) for $e_i^* = e_i^L$, i.e. if the partitioning of NO_x remains unaffected after removing the background, which is assumed in our analysis (see discussion in Sect. 4.1.3).

The terms containing V^0 can be summarized as:

$$\Delta S^{NO_2} = S^{LNO_2} + V^0 \cdot (E^{*,0} - E^0)) \tag{A3}$$

E^0 is the sensitivity to background NO_x under background (clear) conditions. $E^{*,0}$ is the sensitivity to background NO_x (with modified profile $p^{\sim 0}$) under modified (clouded) conditions (e^*). The difference $E^{*,0}$–E^0 reflects the change of sensitivity for background NO_x due to the change in viewing conditions (clouds) for thunderstorms.

Note that

1. the stratosphere plays no role in our considerations, since here we have no change of sensitivity ($E^{*,0} \approx E^0$).

2. the second term of Eq. (A3) can be both, positive and negative, depending on the change of sensitivity. In general, we expect a shielding effect ($E^{*,0} < E^0$), but convection could also increase the net sensitivity ($E^{*,0} > E^0$).

3. for relatively low values of S^{LNO_2} and high values of V^0, the shielding can actually lead to a negative response ($\Delta S^{NO_2} < 0$) to lightning NO_x!

4. for scenes that are dominated by lightning NO_x, the second term of Eq. (A3) is negligible, and

$$\Delta S^{NO_2} \approx S^{LNO_2} \tag{A4}$$

for low V^0.

Acknowledgements. This project is funded by the DFG (Deutsche Forschungsgemeinschaft, German research society). The authors thank Tim Deutschmann for the valuable work on the RTM model McArtim and support in running it.

MAX-PLANCK-GESELLSCHAFT

This Open Access Publication is financed by the Max Planck Society.

References

Beirle, S., Platt, U., Wenig, M., and Wagner, T.: NO_x production by lightning estimated with GOME, Adv. Space Res., 34(4), 793–797, 2004.

Beirle, S., Spichtinger, N., Stohl, A., Cummins, K. L., Turner, T., Boccippio, D., Cooper, O. R., Wenig, M., Grzegorski, M., Platt, U., and Wagner, T.: Estimating the NO_x produced by lightning from GOME and NLDN data: a case study in the Gulf of Mexico, Atmos. Chem. Phys., 6, 1075–1089, 2006, http://www.atmos-chem-phys.net/6/1075/2006/.

Boccippio, D. J., Cummins, K. L., Christian, H. J., and Goodman, S. J.: Combined Satellite- and Surface-Based Estimation of the Intracloud-Cloud-to-Ground Lightning Ratio over the Continental United States, Mon. Weather Rev., 129, 108–122, 2000.

Boersma, K. F., Eskes, H. J., Meijer, E. W., and Kelder, H. M.: Estimates of lightning NO_x production from GOME satellite observations, Atmos. Chem. Phys., 5, 2311–2331, 2005, http://www.atmos-chem-phys.net/5/2311/2005/.

Bovensmann, H., Burrows, J. P., Buchwitz, M., Frerick, J., Noël, S., Rozanov, V. V., Chance, K. V., and Goede, A. P. H.: SCIAMACHY: Mission objectives and measurement modes, J. Atmos. Sci., 56(2), 127–150, 1999.

Burrows, J., Weber, M., Buchwitz, M., Rozanov, V. V., Ladstädter-Weissenmayer, A., Richter, A., de Beek, R., Hoogen, R., Bramstedt, K., Eichmann, K.-U., Eisinger, M., and Perner, D.: The Global Ozone Monitoring Experiment (GOME): Mission concept and first scientific results, J. Atmos. Sci., 56, 151–175, 1999.

Christian, H. J., Blakeslee, R. J., Boccippio, D. J., et al.: Global frequency and distribution of

Title Page
Abstract Introduction
Conclusions References
Tables Figures
◄ ►
Back Close
Full Screen / Esc
Printer-friendly Version
Interactive Discussion

lightning as observed from space by the Optical Transient Detector, J. Geophys. Res., 108, 4005, doi:10.1029/2002JD002347, 2003.

DeCaria, A. J., Pickering, K. E., Stenchikov, G. L., Scala, J. R., Stith, J. L., Dye, J. E., Ridley, B. A., and Laroche, P.: A cloud-scale model study of lightning-generated NO_x in an individual thunderstorm during STERAO-A, J. Geophys. Res., 105, 11 601–11 616, 2000.

DeCaria, A. J., Pickering, K. E., Stenchikov, G. L., and Ott, L. E.: Lightning-generated NO_x and its impact on tropospheric ozone production: A three-dimensional modeling study of a Stratosphere-Troposphere Experiment: Radiation, Aerosols and Ozone (STERAO-A) thunderstorm, J. Geophys. Res., 110, D14303, doi:10.1029/2004JD005556, 2005.

Deutschmann, T., and T. Wagner, TRACY-II Users manual, http://joseba.mpch-mainz.mpg.de/Strahlungstransport.htm, 2006.

Deutschmann, T.: The RTM McArtim, Diploma Thesis, Universität Heidelberg, in progress, 2008.

Fehr, T., Höller, H., and Huntrieser, H.: Model study on production and transport of lightning-produced NO_x in a EULINOX supercell storm, J. Geophys. Res., 109, D09102, doi:10.1029/2003JD003935, 2004.

Hild, L., Richter, A., , Rozanov, V., and Burrows, J. P.: Air Mass Calculations for GOME Measurements of lightning-produced NO_2, Adv. Space Res., 29(11), 1685–1690, 2002.

Jöckel, P., Tost, H., Pozzer, A., Brühl, C., Buchholz, J., Ganzeveld, L., Hoor, P., Kerkweg, A., Lawrence, M. G., Sander, R., Steil, B., Stiller, G., Tanarhte, M., Taraborrelli, D., van Aardenne, J., and Lelieveld, J.: The atmospheric chemistry general circulation model ECHAM5/MESSy1: consistent simulation of ozone from the surface to the mesosphere, Atmos. Chem. Phys., 6, 5067–5104, 2006, http://www.atmos-chem-phys.net/6/5067/2006/.

von Kuhlmann, R., Lawrence, M. G., Crutzen, P. J., and Rasch, P. J.: A model for studies of tropospheric ozone and nonmethane hydrocarbons: Model description and ozone results, J. Geophys. Res., 108, doi:10.1029/2002JD002893, 2003.

Labrador, L. J., von Kuhlmann, R., and Lawrence, M. G. : The effects of lightning-produced NO_x and its vertical distribution on atmospheric chemistry: sensitivity simulations with MATCH-MPIC, Atmos. Chem. Phys., 5, 1815–1834, 2005, http://www.atmos-chem-phys.net/5/1815/2005/.

Levelt, P. F., van den Oord, G. H. J., Dobber, M. R., Malkki, A., Visser, H., de Vries, J., Stammes, P., Lundell, J. O. V., and Saari, H.: The ozone monitoring instrument, IEEE T. Geosci. Remote, 44, 5, 1093–1101, 2006.

Marchuk, G., Mikhailov, G., Nazaraliev, M., Darbinjan, R., Kargin, B., and Elepov, B.: The Monte Carlo Methods in Atmospheric Optics, Springer-Verlag Berlin, 208 pp., 1980.

Marshak, A., Davis, A., Cahalan, R. F., and Wiscombe, W., Nonlocal Independent Pixel Approximation: Direct and Inverse Problems, IEEE T. Geosci. Remote, 36, 1, 192–205, 1998.

Martin R. V., Sauvage, B., Folkins, I., Sioris, C. E., Boone, C., Bernath, P., Ziemke, J.: Space-based constraints on the production of nitric oxide by lightning, J. Geophys. Res., 112, D09309, doi:10.1029/2006JD007831, 2007.

Ott, L. E., Pickering, K. E., Stenchikov, G. L., Huntrieser, H., and Schumann, U.: Effects of lightning NO_x production during the 21 July European Lightning Nitrogen Oxides Project storm studied with a three-dimensional cloud-scale chemical transport model, J. Geophys. Res., 112, D05307, doi:10.1029/2006JD007365, 2007.

Pickering, K. E., Wang, Y., Tao, W.-K., Price, C., and Müller, J.-F.: Vertical distributions of lightning NO_x for use in regional and global chemical transport models, J. Geophys. Res., 103, 31 203–31 216, 1998.

Pierce, E. T.: Latitudinal variation of lightning parameters, J. Appl. Metalwork, 9, 194–195, 1970.

Platt, C. M. R.: A parameterization of the visible extinction coefficitent of ice clouds in terms of the ice/water content, J. Atmos. Sci., 54, 2083–2098, 1997.

Price, C. and Rind, D.: A simple lightning parameterization for calculating global lightning distributions, J. Geophys. Res., 97, 9919–9933, 1992.

Price, C. and Rind, D.: What determines the cloud-to-ground lightning fraction in thunderstorms?, Geophys. Res. Lett., 20, 463–466, 1993.

Ray, P. S., MacGorman, D. R., Rust, W. D., Taylor W. L., and Walters Rasmussen, L., Lightning location relative to storm structure in a supercell and a multicell storm, J. Geophys. Res., 92, 5713–5724, 1987.

Ridley, B. A., Dye, J. E., Walega, J. G., Zheng, J., Grahek, F. E., and Rison, W.: On the production of active nitrogen by thunderstorms over New Mexico, J. Geophys. Res., 101, 20 985–21 005, 1996.

Rodger, C. J., Werner, S., Brundell, J. B., Lay, E. H., Thomson, N. R., Holzworth, R. H., and Dowden, R. L.: Detection efficiency of the VLF World-Wide Lightning Location Network (WWLLN): Initial case study, Ann. Geophys., 24, 3197–3214, 2006, http://www.ann-geophys.net/24/3197/2006/.

Salzmann, M., Lawrence, M. G., Phillips, V. T. J., and Donner, L. J.: Modelling tracer transport by a cumulus ensemble: Lateral boundary conditions and large-scale ascent, Atmos. Chem. Phys., 4, 1797–1811, 2004, http://www.atmos-chem-phys.net/4/1797/2004/.

Salzmann, M., Lawrence, M. G., Phillips, V. T. J., and Donner, L. J.: Cloud system resolving model study of the roles of deep convection for photo-chemistry in the TOGA COARE/CEPEX region, Atmos. Chem. Phys., 8, 2741–2757, 2008, http://www.atmos-chem-phys.net/8/2741/2008/.

Schumann, U. and Huntrieser, H.: The global lightning-induced nitrogen oxides source, Atmos. Chem. Phys., 7, 3823–3907, 2007, http://www.atmos-chem-phys.net/7/3823/2007/.

Skamarock, W. C., Klemp, J. B., and Dudhia, J: Prototypes for the WRF (Weather Research and Forecasting) model, in: Preprints, Ninth Conf. Mesoscale Processes, J11–J15 pp., Am. Meteor. Soc., Fort Lauderdale, FL, 2001.

Tost, H., Jöckel, P., and Lelieveld, J.: Lightning and convection parameterisations – uncertainties in global modelling, Atmos. Chem. Phys., 7, 4553–4568, 2007, http://www.atmos-chem-phys.net/7/4553/2007/.

Wagner, T., Burrows, J. P., Deutschmann, T., Dix, B., von Friedeburg, C., Frie, U., Hendrick, F., Heue, K.-P., Irie, H., Iwabuchi, H., Kanaya, Y., Keller, J., McLinden, C. A., Oetjen, H., Palazzi, E., Petritoli, A., Platt, U., Postylyakov, O., Pukite, J., Richter, A., van Roozendael, M., Rozanov, A., Rozanov, V., Sinreich, R., Sanghavi, S., and Wittrock, F.: Comparison of box-air-mass-factors and radiances for Multiple-Axis Differential Optical Absorption Spectroscopy (MAX-DOAS) geometries calculated from different UV/visible radiative transfer models, Atmos. Chem. Phys., 7, 1809–1833, 2007, http://www.atmos-chem-phys.net/7/1809/2007/.

Wagner, T., Beirle, S., Deutschmann, T., Eigemeier, E., Frankenberg, C., Grzegorski, M., Liu, C., Marbach, T., Platt, U., and Penning de Vries, M.: Monitoring of atmospheric trace gases, clouds, aerosols and surface properties from UV/vis/NIR satellite instruments, J. Opt. A., Pure Appl. Opt., 10, 104019, doi:10.1088/1464-4258/10/10/104019, 9 pp., 2008.

Webster, P. J. and Lukas, R.: TOGA COARE: The Coupled Ocean-Atmosphere Response Experiment, B. Am. Meteorol. Soc., 73, 1377–1416, 1992.

Wenig, M., Kühl, S., Beirle, S., Bucsela, E., Jähne, B., Platt, U., Gleason, J., and Wagner, T.: Retrieval and analysis of stratospheric NO_2 from the Global Ozone Monitoring Experiment, J. Geophys. Res., 109, D04315, doi:10.1029/2003JD003652., 2004.

Table 1. Effect of modifications of RTM settings on the resulting sensitivity for the first OTS shown in Fig. 7 (left). The resulting sensitivity for standard settings is 0.306.

	SZA=		SSA=		g=		Ground albedo=		Extinction coefficient	
Modification	40°	60°	0.9999	0.999	0.8	0.9	0%	10%	*0.5	*2
Sensitivity	0.313	0.334	0.305	0.301	0.287	0.339	0.236	0.357	0.365	0.266
Relative change	+2%	+9%	−0%	−2%	−6%	+11%	−23%	+17%	+19%	−13%

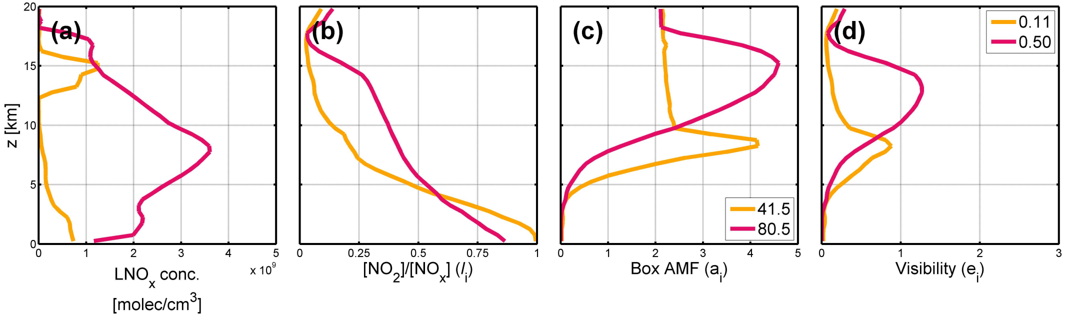

Fig. 1. Two illustrative examples from the simulation. The first (orange) represents a typical "C-shape" profile. The second (red) reflects a high LNO$_x$ column in the core region. **(a)** Profiles of LNO$_x$ concentration. **(b)** NO$_2$/NO$_x$ ratio (l_i). **(c)** box-AMFs (a_i) as calculated by the McArtim RTM. The numbers in the legend are the respective cloud optical depth. **(d)** Resulting Visibility (e_i). The resulting Sensitivities E are given in the legend in (d).

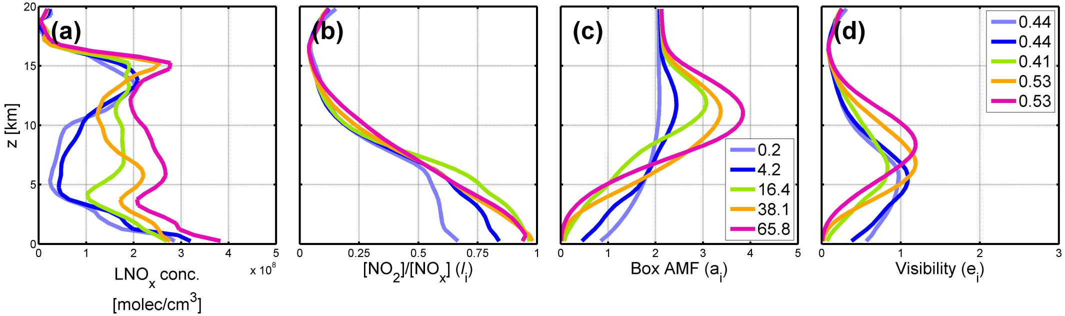

Fig. 2. Mean profiles for the scenes classified in different regimes (I-V) according to COT (see text). Panels as in Fig. 1. Note the change of scale in **(a)** compared to Fig. 1. "Mean" l_i is defined as mean([NO$_2$])/mean([NO$_x$]) (the NO$_2$ and NO$_x$ concentrations in layer i are averaged across all scenes of the respective regime).

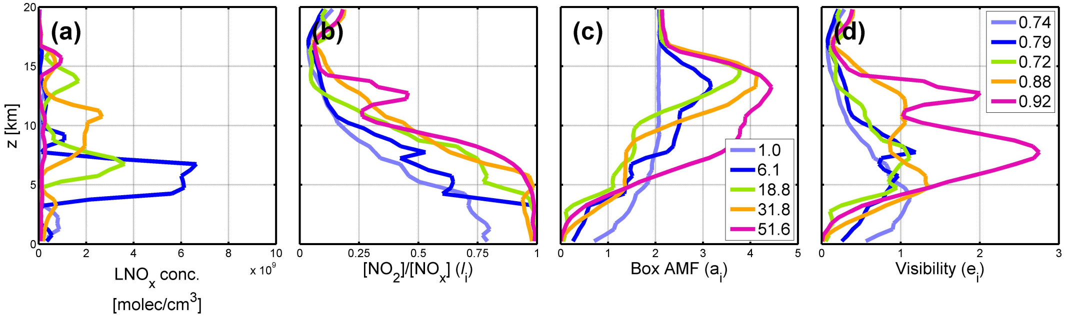

Fig. 3. Sample profiles of the cases with highest sensitivity for the five regimes. Colours as in Fig. 2. Note the change of scale in **(a)**.

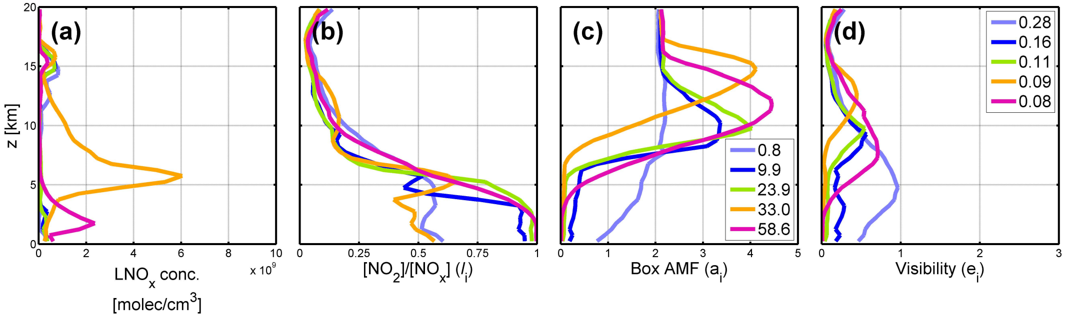

Fig. 4. Sample profiles of the cases with lowest sensitivity for the five regimes. Colours as in Fig. 2.

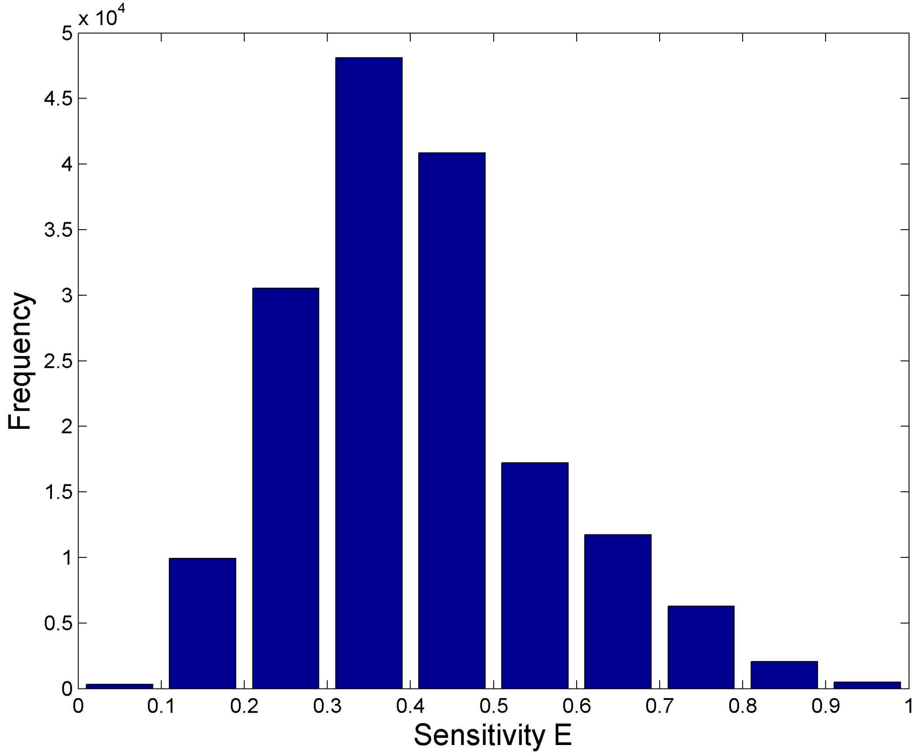

Fig. 5. Frequency distribution of the resulting sensitivities. 81% of all individual sensitivities are between 0.2 and 0.6.

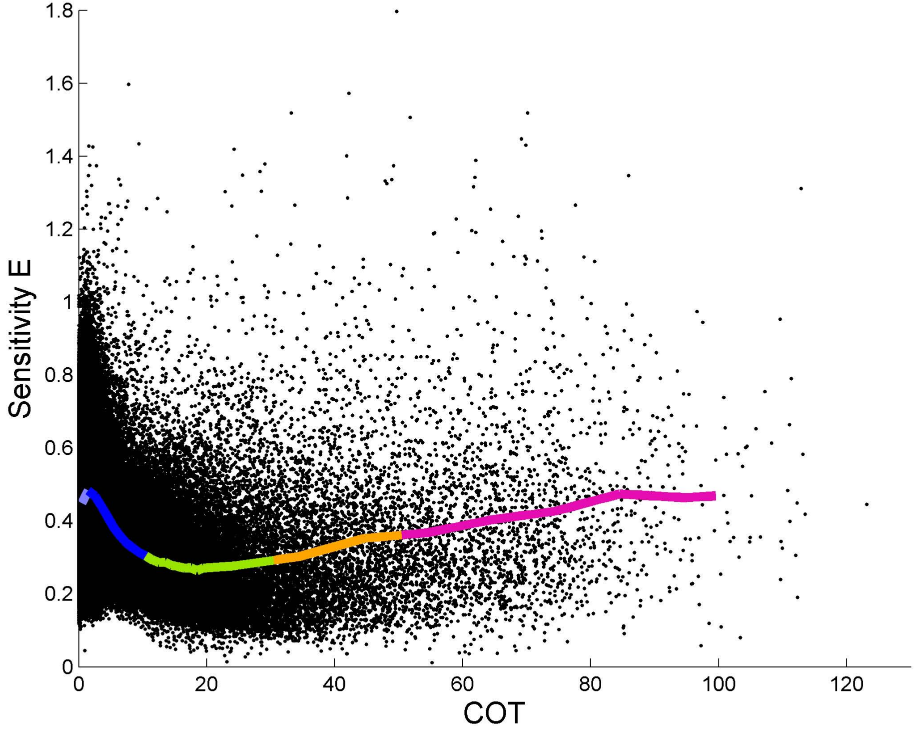

Fig. 6. Scatterplot of sensitivity E versus cloud optical thickness for all analyzed scenes. The correlation coefficient is $R=-0.27$. The curve shows the mean sensitivity for binned COT (ΔCOT=1 for COT<=20 and 10 above). The colour indicates the regime (colours as in Fig. 2).

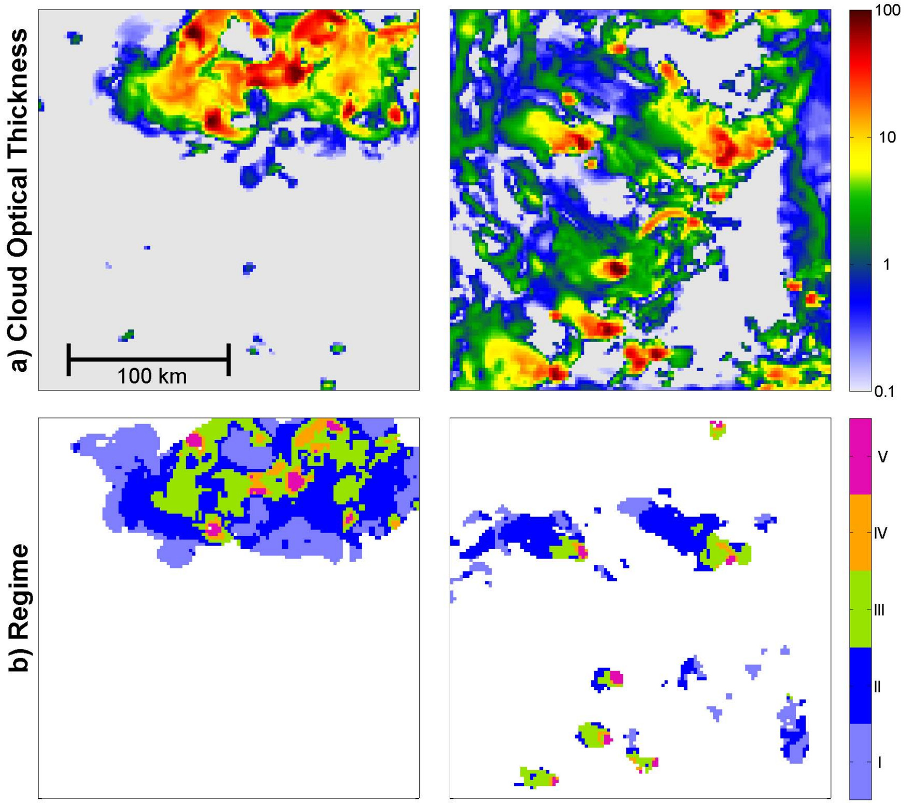

Fig. 7. Maps of **(a)** COT and **(b)** regime classification for two illustrative OTSs that represent a case of low sensitivity (left column, E_{total}=0.31), and high sensitivity (right column, E_{total}=0.66), respectively. In (b), pixels with $V^{LNO_x}<10^{14}$ molec/cm^2 are masked out.

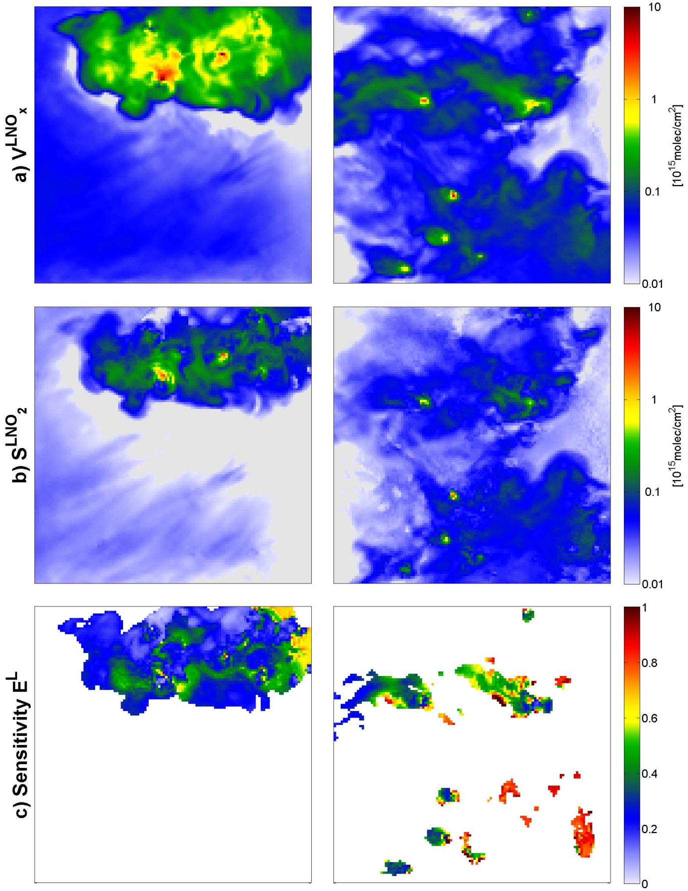

Fig. 8. Maps of **(a)** V^{LNO_x}, **(b)** S^{LNO_2}, and **(c)** sensitivity E^L, for the two OTSs shown in Fig. 7. In (c), pixels with $V^{LNO_x} < 10^{14}$ molec/cm^2 are masked out.

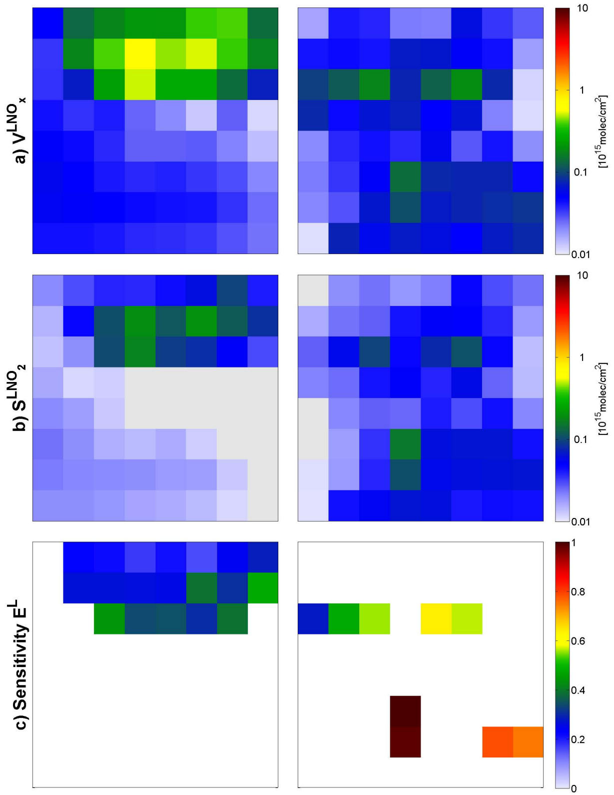

Fig. 9. As Fig. 8, but for reduced spatial resolution (30×30 km^2). Note that the spatial mean S^{LNO_2} has been weighted by the respective intensity of the single scenes to simulate the satellite measurement.

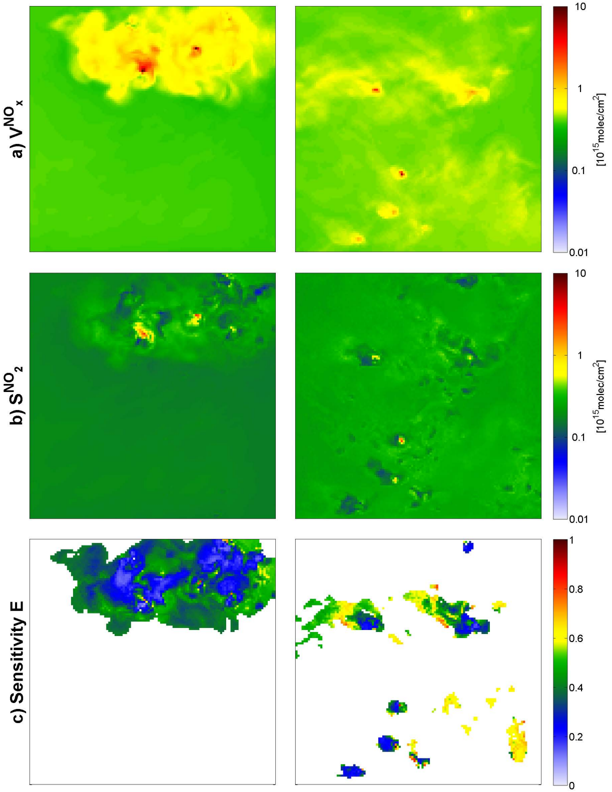

Fig. 10. As Fig. 8, but for the non-corrected columns V^{NO_x} **(a)** and S^{NO_2} **(b)**. Panel **(c)** displays sensitivities $E=S^{NO_2}/V^{NO_x}$ of total columns (Eq. 9), while Fig. 8c displays $E^L = S^{LNO_2}/V^{LNO_x}$ (Eq. 12). Due to the rather low LNO_x columns, the shielding of background NO_x is clearly visible for some scenes in (b), leading to a negative response of ΔS^{NO_2} to lightning. Note, however, that there are also regions where E is higher than E^L. Total sensitivities from total columns are 0.40 and 0.57, respectively.